

Flexible Organic Field-Effect Transistors Using Barium Titanate as Temperature-Sensitive Dielectric Layer



Suman Mandal and Dipak K. Goswami

1 Introduction

Over the last few decades, organic field-effect transistors (OFETs) have drawn significant interests among the researchers due to their potential applications in radio frequency identification tag (RFID) [1, 2], nonvolatile memory device [3–5], display technology [6, 7], integrated circuit [8–10], electronic skin [11, 12], and in various sensors and detectors [13–15]. Flexibility and solution processability make the devices unique for many cost-effective large-scale innovative wearable applications. However, these devices suffer from poor field-effect carrier mobility due to weak Van der Waals interaction between organic semiconducting molecules and the interface roughness. Moreover, the device performance depends on several other parameters, like Schottky barrier height, the thickness of the dielectric and semiconducting layers, annealing temperature, and growth temperature [16–19]. Many researchers have made efforts to improve device performance and the stability by proper selection of materials by optimizing the growth of various films. Besides, when OFETs are used as sensors, either the semiconducting or gate dielectric layer is used as a sensing layer [20–22]. In this work, we have used a temperature sensing material in the gate dielectric layer. OFETs-based sensors are efficient due to their multiparameter accessibility and amplification capability of the sensing signals, unlike chemisorption-based sensors. Here, we have focused on the fabrication of ultrafast, high-precision flexible temperature sensor through engineering the semiconductor/dielectric interface by controlling different growth parameters.

S. Mandal · D. K. Goswami (✉)

Organic Electronics Laboratory, Department of Physics, Indian Institute of Technology Kharagpur, Kharagpur, West Bengal, India

e-mail: dipak@phy.iitkgp.ac.in

© The Author(s), under exclusive license to Springer Nature Switzerland AG 2021

113

A. G. Roca et al. (eds.), *Surfaces and Interfaces of Metal Oxide Thin Films,*

Multilayers, Nanoparticles and Nano-composites,

https://doi.org/10.1007/978-3-030-74073-3_5

Temperature is one of the essential physiological parameters in the human body. Continuous monitoring of the body temperature is a preliminary step to track different health-related critical problems, such as febrile seizure and epilepsy, requiring more accurate measurement of body temperature at a fast rate [18–20, 23]. Even the precise monitoring of the body temperature change in women during the complete menstruation cycle can predict the ovulation time more accurately [24, 25]. Besides, the highly ambient-stable flexible temperature sensor can find applications in food and medicine preservation technology [26, 27]. Different types of flexible temperature sensors suitable for wearable applications are also demonstrated in the literature. Such sensors are mainly capacitive or resistive types, where a temperature-sensitive material is incorporated into the devices. The changes in capacitance or resistance due to temperature variation are measured to sense temperature [28–33]. However, to improve the sensitivity and precision, OFETs are introduced as another platform, mainly in different wearable applications. OFET integrated with thermistor also has been widely used for wearable temperature sensing applications [34–36]. However, the integration of thermistor can increase the complexity of the fabrication process. For the fabrication of the OFET-based temperature sensor, a temperature-sensitive material is used as a dielectric layer in the device fabrication. The semiconducting channel layer can also be used as sensing materials in OFETs [37, 38]. However, such sensors suffer from higher response and recovery time that limits their applications. Nevertheless, these devices are operated at high voltage which prevents its usage from wearable applications [34–38].

We have introduced hexagonal barium titanate nanocrystals (h-BTNCs) as temperature sensing materials for the fabrication of OFET-based temperature sensors. Barium titanate (BaTiO_3 , BTO) is a ferroelectric material that exhibits high dielectric constant and low dielectric loss due to its spontaneous electric polarization. BTO is known to have different crystallographic structures, like rhombohedral, orthorhombic, tetragonal, and cubic at different temperature ranges. The dielectric constant of this material depends on the crystallographic structures. The difficulty to obtain these crystallographic phases is that high-temperature annealing process. It is not easy to grow smooth thin films with these materials as high-temperature annealing makes larger crystallite sizes and film grown with such materials make the film rough. Therefore, BTO in the crystalline phase has not been used for the fabrication of high-performance OFETs. In this work, we have synthesized the hexagonal nanocrystals of BTO within the amorphous phase. This material requires a low processing temperature ($\sim 80^\circ\text{C}$). Besides, we can grow highly smooth interfaces and can fabricate OFETs with low operation voltage.

2 Experimental Section

Materials Synthesis The solgel method was adopted to synthesis the h-BTNCs solutions, where barium acetate and titanium butoxide were used as precursor materials. Glacial acetic acid and 2-methoxyethanol material were used as the solvent.

Initially, barium acetate was vigorously stirred to dissolved in the solvent for 3 h using a magnetic stirrer at room temperature. Titanium butoxide was added to the reaction mixture drop-by-drop by maintaining the stoichiometric ratio. The solution was stirred again for another 3 h at room temperature. Finally, the ambient-stable h-BTNCs solution was prepared and used as a dielectric material in OFETs.

OFETs Fabrications In conventional OFETs, two metal electrodes such as source and drain are used to connect the organic semiconductor (channel). The other electrode (gate) capacitively coupled through a dielectric layer is used to modulate the current that flows in between source to drain electrode through the channel. The OFETs were fabricated in bottom-gate-top-contact (BGTC) configurations on the glass as well as in the PET substrate. A thin film of aluminum with thickness 125 (± 10) nm was deposited on a clean substrate using a thermal evaporation chamber ($\sim 4 \times 10^{-6}$ mbar). The aluminum surface was anodized at room temperature by using an anodic oxidation method to get a 15 nm thin alumina film used together with h-BTNCs as a bilayer dielectric system of the devices. In this anodization process, citric acid was used as electrolyte material and platinum wire as a cathode material. Source meter (Keithley 2450) was connected to the anode and cathode terminal to provide a constant current density for this anodic oxidation process. After anodization, the anodic surface was flushed with DI water and subsequently dried using hot air. The h-BTNCs sol was spin-coated on top of alumina surface at 3000 rpm for 60 s and subsequently annealed at various substrate temperatures (from 40 °C to 120 °C) for 90 min to get a thin film of around 50 nm thickness. After that, a pentacene film of thickness around 20 nm was deposited under a high vacuum condition ($\sim 2 \times 10^{-6}$ mbar) using organic molecular beam depositing (OMBD) system. Finally, Copper (Cu) film with thickness 60 nm was deposited on top of pentacene film as a source–drain electrode through a shadow mask to get the channel Length (L) and channel width (W) of 30 μm and 2 mm, respectively.

2.1 Device Characterizations

Atomic force microscopy (AFM, Bruker) was used to characterize the surface morphology of each layer of the devices. The thickness of each layer was measured using a 3D surface profilometry. The devices' capacitance and leakage current were characterized in a simple metal–insulator–metal (MIM) structure using a LCR meter (Keysight) and source meters (Keithley 2450). Finally, the variation of drain current with temperature was carried out inside a custom design probe station using two source meters (Keithley 2450). The typical current resolution of the systems is around 1 pA in 1 mA scale and 10 pA in 10 mA current scale.

The field-effect carrier mobility of the devices was extracted from the saturation region by using the following equation.

$$I_D = \frac{W}{2L} \cdot C \cdot \mu \cdot (V_G - V_T)^2 \quad (1)$$

where I_D , C , μ , V_G , and V_T are the drain current, the capacitance of the oxide layer, mobility, gate voltage, and threshold voltage, respectively.

3 Results and Discussions

3.1 Characterization of Temperature-Sensitive h-BTNC Dielectric Material

The dielectric material plays a significant role in deciding the device's performance. The gate capacitance is dependent on the thickness of the dielectric layer and the dielectric constant of the material. The operating voltage is directly related to this parameter. For OFETs, the charge conduction occurs mostly through the semiconductor dielectric interface. Therefore, the roughness of the dielectric layer defines the conducting channel. Besides, the leakage current of the device is decided by the quality of the dielectric film. We have used the solution-processable h-BTNCs materials as one of the dielectric layers of the bilayer dielectric system. The h-BTNCs sol was spin-coated on alumina film and subsequently annealed at 80 °C to prepare a thin film. The elemental composition of the film was analyzed from x-ray photoelectron spectroscopy (XPS). The emission spectra of Ba 3d, Ti 2p, and O 1s state from the h-BTNC thin film are shown in Fig. 1a–d. The corresponding binding energy as observed from Ba3d5/2, Ba3d3/2, Ti2p3/2, Ti2p1/2, and O1s are 778.99 eV, 794.22 eV, 457.53 eV, 463.25 eV, and 529.02 eV, respectively. The values are summarized in Table 1. The presence of residual carbon contamination also has been observed in the O1s spectra at 530.26 eV [19, 39].

High-resolution transmission electron microscopy (HRTEM) measurements were carried out to study the structural information of h-BTNC films. We have observed hexagonal nanocrystalline flakes within the amorphous phase. The low magnification bright-field TEM image of the BTO film is shown in Fig. 2a [19]. The inset Fig. 2a shows the crystallites present in the h-BTNC film taken from Fig. 2a. The typical dimensions of the crystallites are about ~ 50 nm in length and 5–10 nm in diameter. The Fig. 2b and 2c present the selected area diffraction pattern (SAD) taken from the circular regions, marked by I and J, which indicate the amorphous phase of the film. The indexing of the SAD pattern has been done by using the lattice parameters of hexagonal close-packed structure (lattice parameters, $a = 5.73 \text{ \AA}$, and $c = 14.01 \text{ \AA}$). The corresponding interplanar spacings (d-spacing) observed from the SAD pattern are 3.50 Å and 2.05 Å, and these are corresponding to (004) and (106) plane of hexagonal barium titanate (JCPDS # 89-8119). The HRTEM image of h-BTNC film is shown in Fig. 2d, and the inset Fig. 2d shows the Fourier-filtered image taken from a dotted region in Fig. 2a. The measured d-spacing

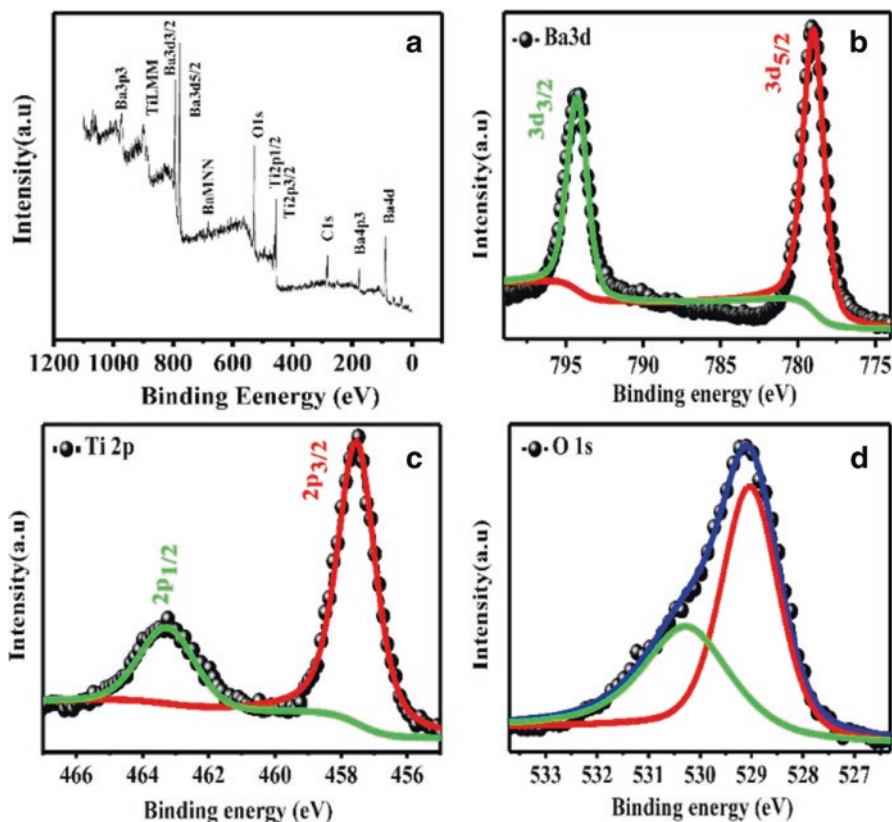


Fig. 1 XPS spectra taken from the h-BTNCs film. (a) presents survey scan, and (b), (c), and (d) depict the high-resolution scan of Ba3d, Ti2p, and O1s, respectively. (Reprinted from [19] © 2019 American Chemical Society)

Table 1 Binding energy of various elements presents in h-BTNC film

	States	Binding energy (eV)
Ba	3d _{5/2}	778.99
	3d _{3/2}	794.22
Ti	2p _{3/2}	457.53
	2p _{1/2}	463.25
O	1s	529.02

calculated from the HRTEM image is around 3.50 Å that corresponds to the (004) plane.

Characterization of Pentacene Layer Pentacene film grown on BTO film has been used as a semiconducting layer. The molecular ordering of pentacene molecules significantly depends on the roughness of the surfaces on which the film is

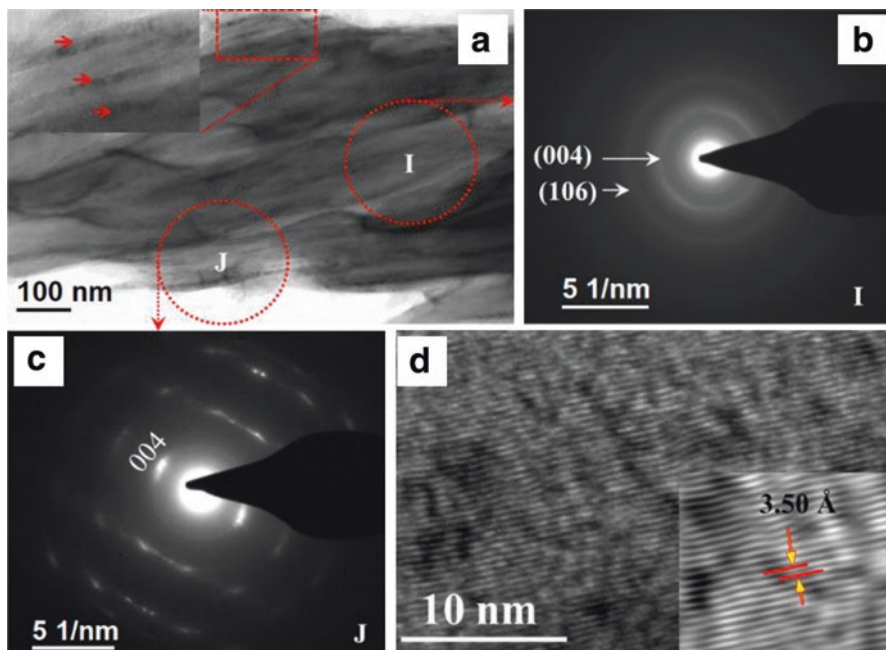


Fig. 2 (a) Presents the TEM image of h-BTNC films. (b) and (c) shows the selected area diffraction pattern (SAD) of it from the circular regions I and J, respectively. (d) presents the corresponding HRTEM image with a Fourier-filtered image in the inset taken from a dotted box marked in (a). (Reprinted from [19] © 2019 American Chemical Society)

growing. The formation of crystalline dendrite structure for the pentacene films is typical. However, it has been shown that pentacene films become amorphous if the surface roughness of the substrate is very high [40, 41]. X-ray diffraction (XRD) measurements were carried out on pentacene/h-BTNC/Al₂O₃/Al/glass and pentacene/h-BTNC/Al₂O₃/Al/PET films. The corresponding diffraction patterns are shown in Fig. 3a–b, respectively. The inset of the figure shows a narrow scan, where 2θ was varying from 5 to 20 degrees. The dendrite structures have two different crystallographic phases, such as thin film and bulk phases. The crystallite size of the thin-film phase and bulk phase has been calculated from Fig. 3c and 3d,, which are the first peak of Fig. 3a and 3b, respectively. The peak (001') and (001) correspond to the thin-film and bulk phase of the pentacene film's polymorphous nature [42]. We have calculated the mean crystallite size (τ) using the Scherrer equation for both films. The crystallites size for the thin-film phase was 9.22 Å and 11.88 Å for the films grown on h-BTNC/Al₂O₃/Al/ glass and h-BTNC/Al₂O₃/Al/ PET, respectively, as given in Table 2.

It has been found that the pentacene films grown on h-BTNC/Al₂O₃/Al/ PET have higher τ in comparison to the samples grown on the glass substrates. It implies that the PET substrate-based film has higher grain boundaries. Therefore, the grain

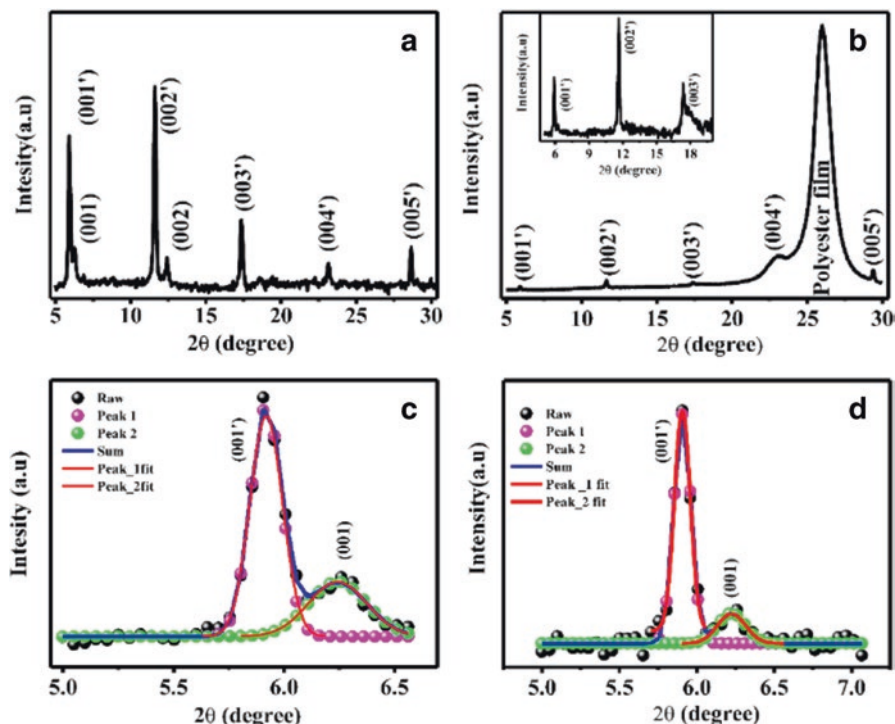


Fig. 3 (a) and (b) show x-ray diffraction pattern from pentacene/BaTiO₃/Al₂O₃/Al/glass and pentacene/BaTiO₃/Al₂O₃/Al/PET, respectively. The inset Figure shows a narrow 2θ scan from 5 to 20 degrees; (c) and (d) depict the first peak corresponding to the (001') and (001) plane of Figure (a) and (b), respectively. (Reprinted from [19] © 2019 American Chemical Society)

boundary-induced density of defect states is expected to be less in PET substrates. Besides, the higher d-spacing (~ 14.95 Å) for the thin-film phase indicates that the tilt angle of pentacene molecules is more elevated than in the bulk phase [42].

4 Optimization of Growth of h-BTNC Films

Thickness Optimization of h-BTNC Film The charge accumulation at the conducting channel depends on the gate dielectric capacitance, which crucially depends on the layer's thickness. The device's output current decreases for a particular applied gate bias by increasing the thickness of the gate dielectric. However, a thin dielectric layer increases the leakage current of the device. We have optimized the thickness of the dielectric layer to achieve higher carrier mobility. The film's thickness has been varied by varying the spinning speed of spin coater from 1000 rpm to 4000 rpm. Following the growth, we annealed the films at 80 °C for 90 min. These films were used for the fabrication of the OFETs. The output charac-

Table 2 Various parameters obtained from XRD analysis of pentacene film grown on top of h-BTNC/Al₂O₃/Al/glass and h-BTNC/Al₂O₃/Al/PET

	FWHM (β)	Theta (θ)	τ (glass)	τ (plastic)	d ₀₀₁ spacing
Thin-Film phase	0.167 (Glass)	2.955 (Glass)	9.22 Å	11.88 Å	14.95 Å (Glass)
	0.129 (Plastic)	2.953 (Plastic)			14.97 Å (Plastic)
Bulk phase	0.313 (Glass)	3.130 (Glass)	4.93 Å	7.37 Å	14.12 Å (Glass)
	0.209 (Plastic)	3.110 (Plastic)			14.12 Å (Plastic)

teristics for those devices prepared by spin coating of the h-BTNCs layer with a spinning speed of 1000, 2000, 3000, and 4000 rpm are shown in Fig. 4a–d. The corresponding transfer characteristics and leakage current of the devices are shown in Fig. 4e–f. The characteristics of the devices grown with 3000 rpm are shown in Fig. 4c and 4e, which delivers the best device property. It has been found that the device with h-BTNC films prepared at 3000 rpm shows minimum leakage current but beyond that rpm, the leakage current increases significantly. The typical thickness for the h-BTNC film grown with 3000 rpm is about 55(±10) nm, and the observed operating voltage of the same device is within 1 V.

Roughness Optimization of h-BTNC Films The surface roughness (σ) of the dielectric layer can introduce traps in the conducting channel. Therefore, it is necessary to grow a dielectric film with lower σ . We have optimized the σ of the film to achieve better charge conduction through the channel. Nevertheless, pentacene film's growth on the h-BTNC layer crucially depends on the σ [43, 44]. To control the σ , we have varied the annealing temperature of the film. The surface morphology of this film at different annealing temperatures is shown in Fig. 5a–d. The measured surface roughness at 40 °C, 80 °C, 120 °C, and 160 °C is 0.5 nm, 0.7 nm, 3.0 nm, and 5.3 nm, respectively. We observed that the σ of the film significantly increased at 120 °C and above annealing temperature. In this work, we have considered the annealing temperature as 80 °C, which is also the pentacene film's growth temperature.

Frequency and Temperature-Dependent Capacitance Measurements In this section, we have discussed the effect of frequency and temperature on the gate capacitance. A simple metal–insulator–metal (MIM) structure was fabricated along with the OFET to study the capacitance of the gate dielectric layer. The variation of capacitance with frequency in the bilayer dielectric system is shown in Fig. 6a. We have covered the frequency range from 10 kHz to 500 kHz. The capacitance of the device is almost constant up to about 200 kHz. However, it decreased at a relatively faster rate in the frequency range above 200 kHz. Therefore, the devices can be operated within 200 kHz frequency range with constant capacitance value. The dielectric property of h-BTNC material is sensitive to temperature. Consequently,

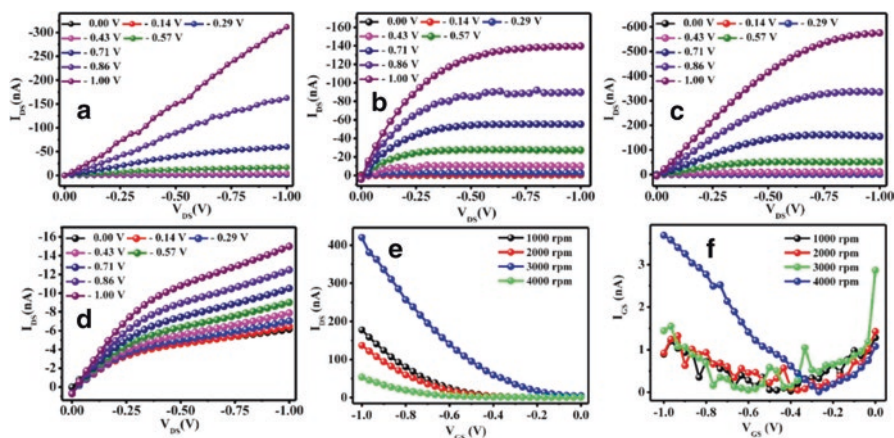


Fig. 4 Thickness optimization of the h-BTNC layer. The output characteristics of the h-BTNC layer deposited at the various spinning speed of (a) 1000, (b) 2000, (c) 3000, and (d) 4000 rpm. (e) and (f) depict transfer characteristics and leakage current of the device, respectively

we measured the temperature-dependent capacitance of the bilayer dielectric system within the temperature range from 20 °C to 50 °C at 100 kHz, as shown in Fig. 6b. The linear temperature dependency has been observed over a range of temperatures from 20 °C to 50 °C with a slope of $2.67 (\pm 0.2) \times 10^{-2}$ (nF/cm²)/°C. This temperature dependency of the h-BTNC film can be exploited to the OFET-based temperature sensors.

5 Optimization of Pentacene Film for OFETs Fabrication

In this section, we have discussed the optimization of pentacene film growth in terms of substrate temperature and film thickness to achieve a better device performance.

Effect of Substrate Temperature on the Growth We have carried out detailed studies of the growth of pentacene film at different substrate temperatures. We have used an organic molecular beam deposition (OMBD) system to grow pentacene films with a fixed growth rate of 3 Å/s at various substrate temperatures, such as 60 °C, 80 °C, 100 °C, and 120 °C. The output and transfer characteristics of typical OFETs grown on glass substrates are shown in Fig. 7a–d and 7e–h. It has been found that at 80 °C, the device offers better performance in terms of device current. We observed maximum carrier mobility for the device prepared at 80 °C substrate temperature. The variation of the device carrier mobility with growth temperature is shown in Fig. 7i.

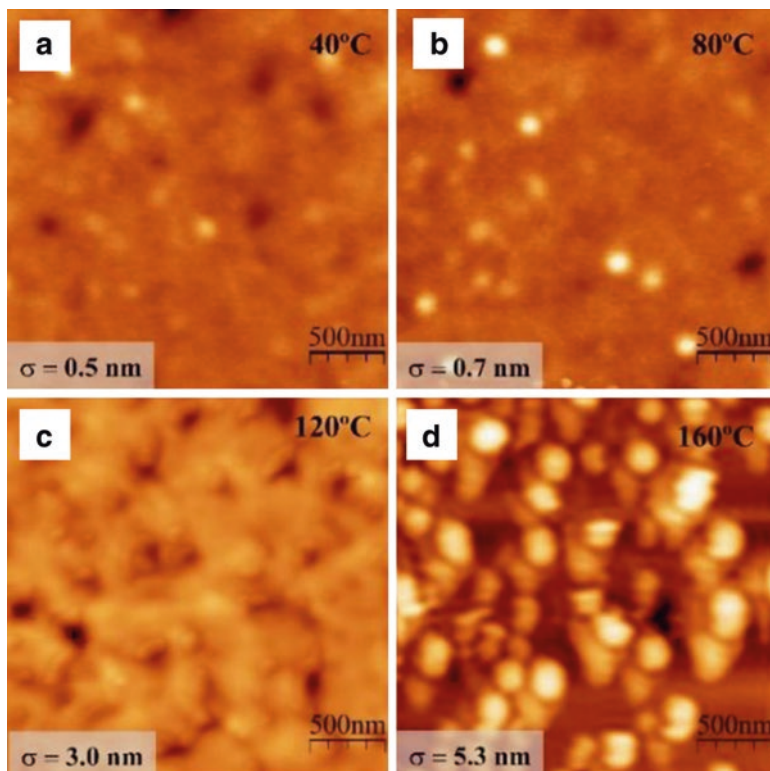


Fig. 5 Presents the effect of annealing on the surface roughness (σ) of h-BTNC film at different temperatures (a) 40 °C, (b) 80 °C, (c) 120 °C, and (d) 160 °C on $\text{Al}_2\text{O}_3/\text{Al}/\text{glass}$. A sudden increase in σ is observed at 120 °C annealing temperature

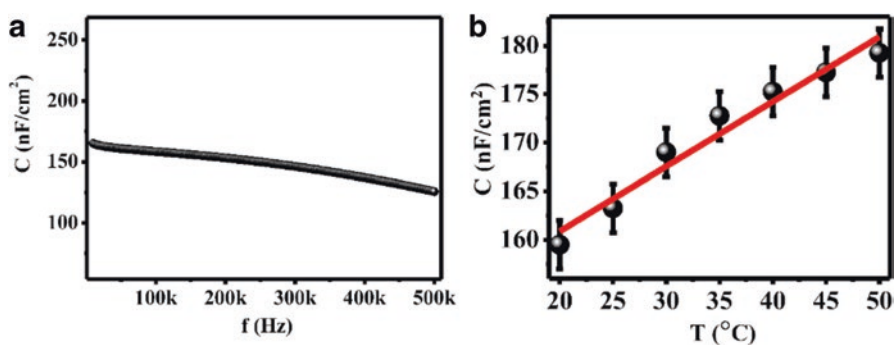


Fig. 6 Presents the capacitance variation of the bilayer dielectric system with (a) frequency from 10 kHz to 500 kHz at room temperature and (b) temperature from 20 °C to 50 °C at 100 kHz. (Reprinted from [19] © 2019 American Chemical Society)

Effect of Pentacene Film Thickness The OFETs were fabricated using bottom-gate-top-contact configuration. The active region for charge conduction comprises about a few nm of the dielectric/semiconductor interface. The channel resistance of the device increases with the thickness of the pentacene film. Figure 8a shows the schematic design of a specific device. The thickness of the pentacene layer has been varied from 10 nm to 60 nm during the growth. The devices' transfer characteristics with various thicknesses of pentacene film are presented in Fig. 8b. We have found that the device mobility increases with decreasing the thickness of the pentacene layer up to a thickness of 20 nm. As the thickness increases, the resistances R_1 and R_2 increase as electrons have to travel longer path. Besides, the trap density across the film increases with the thickness. Therefore, charge injection from the contact to the conducting channel is reduced by increasing the thickness of the pentacene film. We have extracted the device mobility from these transfer characteristics. The thickness-dependent mobility variation is shown in Fig. 8c. We have observed that the device's mobility drastically reduced with a pentacene film of thickness above 20 nm. This could be due to poor charge injection to channel from the metal contacts. Therefore, we have considered the thickness of the pentacene layer as 20 nm.

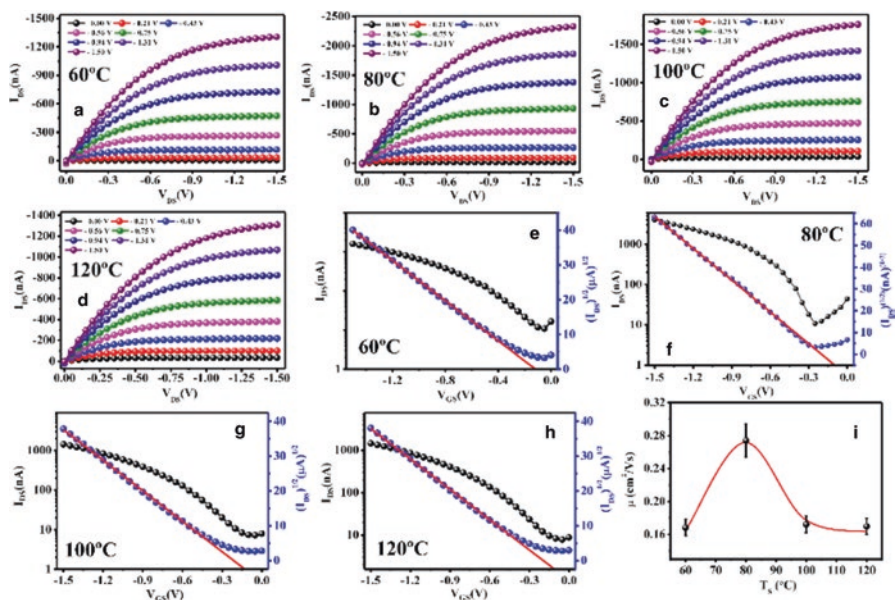


Fig. 7 Substrate temperature optimization during the growth of pentacene films. (a–d) and (e–h) present output and transfer characteristics for substrate temperature variation from 60 °C to 120 °C with an interval of 20 °C, respectively. (i) depicts substrate temperature-dependent mobility variation of those devices

6 Flexible Organic Field-Effect Transistors and Its Characterization

Surface Morphology Characterization of Each Layer The surface morphologies of Al, Al₂O₃/Al, h-BTNC/Al₂O₃/Al, and pentacene/h-BTNC/Al₂O₃/Al grown on the glass and PET substrates have been characterized by using AFM images. The typical surface morphologies of these surfaces are shown in Fig. 9a–d for glass substrates and Fig. 9e–h for PET substrates. The standard root-mean-square (RMS) roughness (σ) of thermally evaporated Al film on glass and PET surfaces is ~ 9.7 and ~ 2.6 nm, respectively, whereas the σ of the Al₂O₃ layer, grown by anodization of Al films, was increased to 11.5 and 3.9 nm for glass and PET substrates, respectively. The h-BTNC film has been spin-coated and subsequently annealed for 90 min at 80 °C for glass and 60 °C for PET substrates. Therefore, the spin-coated h-BTNC films on the rough Al₂O₃ surfaces showed a significant reduction in σ to 0.7 nm and 0.4 nm for glass and PET substrates, respectively. Table 3 summarizes the σ of each of the layers present in glass and PET substrate-based OFETs. The morphology of pentacene films follows the dendrite structures, as observed on any other inert substrate surfaces [40, 41]. The σ of pentacene film was found to be ~ 7 nm and 6.3 nm for glass and PET substrate, respectively. However, the smooth interface between h-BTNC and the pentacene layer improves the charge conduction at the semiconductor/dielectric layer interface.

Device Schematic and Characterizations The bilayer combination of the dielectric layer is used to reduce the leakage current of the devices. The schematic of the OFETs device with the various layers is presented in Fig. 10a. The typical optical images of flexible transistors prepared on 100 μm and 10 μm PET substrate have been shown in Fig. 10b and 10c.

The electrical characterization of the OFETs was carried out at room temperature (~ 25 °C to 30 °C) with a relative humidity condition of 40% to 60%. The output and

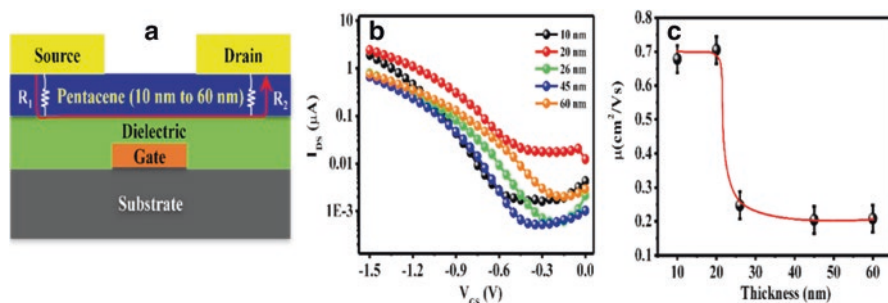


Fig. 8 Thickness dependence of the pentacene layer in OFETs. (a) presents the schematic of the device where the thickness of the pentacene layer varied from 10 nm to 60 nm. (b) shows the pentacene film thickness-dependent transfer characteristics. (c) depicts mobility variation with the thickness of the pentacene layer

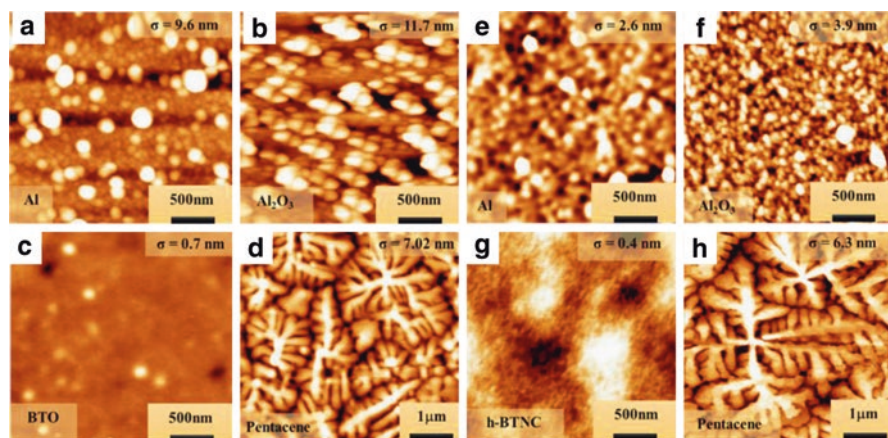


Fig. 9 Surface topography of different layer in OFETs (a) Al, (b) $\text{Al}_2\text{O}_3/\text{Al}$, (c) h-BTNC/ $\text{Al}_2\text{O}_3/\text{Al}$ and (d) pentacene/h-BTNC/ $\text{Al}_2\text{O}_3/\text{Al}$ film on glass substrate (e) Al, (f) $\text{Al}_2\text{O}_3/\text{Al}$, (g) h-BTNC/ $\text{Al}_2\text{O}_3/\text{Al}$, and (h) pentacene/h-BTNC/ $\text{Al}_2\text{O}_3/\text{Al}$ film on PET substrate. (Figure (e–g) reprinted from [19] © 2019 American Chemical Society)

Table 3 Surface roughness (RMS) of Al, $\text{Al}_2\text{O}_3/\text{Al}$, h-BTNC/ $\text{Al}_2\text{O}_3/\text{Al}$, and pentacene /h-BTNC/ $\text{Al}_2\text{O}_3/\text{Al}$ film deposited on glass and PET substrates

Substrate	Al (nm)	Al_2O_3 (nm)	h-BTNC (nm)	Pentacene (nm)
Glass	9.7	11.5	0.7	7.0
PET	2.6	3.9	0.4	6.3

transfer characteristics of the best devices fabricated on glass and PET (100 μm) substrates are shown in Fig. 11a,e and 11b, e, respectively. Device parameters, such as field-effect mobility (μ), the threshold voltage (V_{th}), and on–off ratio, were calculated from the transfer characteristics. The typical values of these parameters are found to be $0.89(\pm 04) \text{ cm}^2/\text{Vs}$, $-0.99(\pm 09) \text{ V}$ and 10^3 , and $1.46(\pm 09) \text{ cm}^2/\text{Vs}$, $-1.05(\pm 06) \text{ V}$ and 10^3 for glass and PET substrate-based OFETs, respectively. The observed operating voltage is about 1.5 V, sufficiently lower and suitable for wearable applications for both set devices. The OFETs fabricated on PET substrates have shown higher carrier mobility. Due to the lower σ of the dielectric layer, the pentacene films exhibit higher crystallinity at initial stage of film growth. The synthesis of h-BTNC sol has been optimized so that we can use it as a dielectric ink for screen printing technology. We have fabricated OFETs on PET substrate using screen printing h-BTNC film on the alumina surfaces. The output and transfer characteristics of screen-printed dielectric-based OFETs are shown in Fig. 11c, f. The mobility, threshold voltage, and on–off ratio calculated from transfer characteristics are $0.70 (\pm 08) \text{ cm}^2/\text{Vs}$, $-1.26 (\pm 06) \text{ V}$, and 10^3 , respectively. For these devices, the carrier mobility decreases with a slight increase in threshold voltage due to the dielectric layer’s thickness variation during screen printing. It implies that the

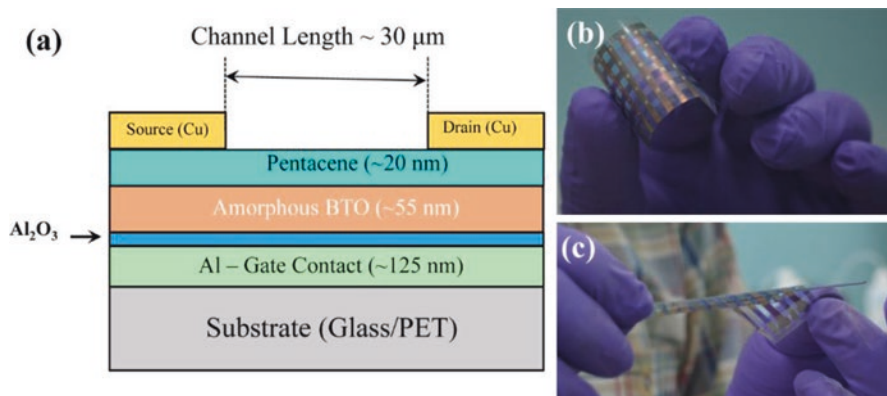


Fig. 10 (a) presents the schematic of OFETs; (b) and (c) depict pictures of the flexible devices on 100 μm and 10 μm thick PET substrates, respectively

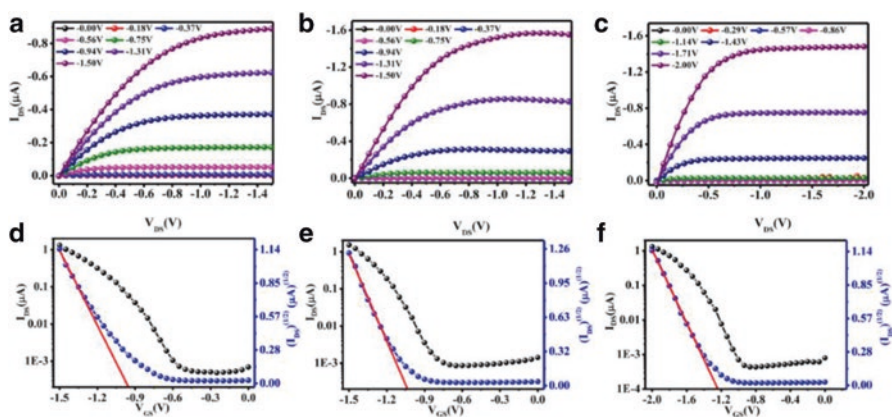


Fig. 11 (a) and (b) present output, and (d), (e) depict transfer characteristics of OFETs on glass and PET substrate, respectively. (c) and (f) show the screen-printed BaTiO₃ film-based OFET on PET substrate measured in ambient condition

h-BTNC sol is also a promising material as a dielectric ink for future printed electronics.

We have fabricated and characterized about over 200 devices on each of the glass and PET substrates. The mobility distribution of these devices is shown in Fig. 12a, b for these devices. We have found that most of the devices offer mobility around $\sim 0.2 \text{ cm}^2/\text{Vs}$ and $\sim 0.25 \text{ cm}^2/\text{Vs}$ for glass and PET substrate-based devices, respectively.

Device Stability in Ambient Condition The devices showed exceptional ambient stability. The carrier mobility of a single OFETs, kept under ambient conditions at a temperature between 25–30 $^\circ\text{C}$ and relative humidity of 50–70%, was monitored over 8 months. We selected a better device with $0.5 \text{ cm}^2/\text{Vs}$ carrier mobility for this

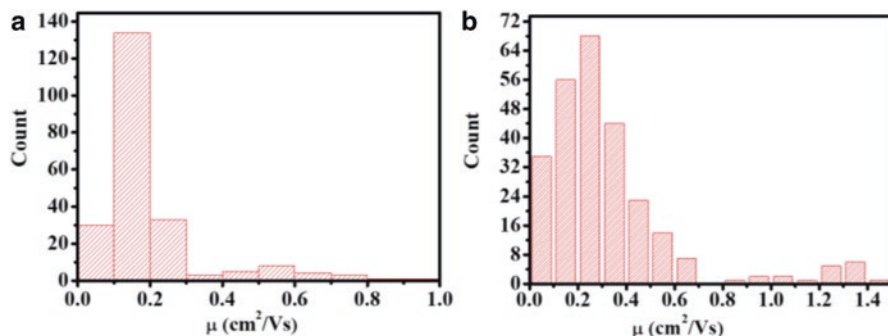


Fig. 12 Histogram of the mobility distribution of devices on top of (a) glass substrates and (b) PET substrates

study. The variation of carrier mobility with time in days is shown in Fig. 13a. We have shown the corresponding transfer characteristics for this device in Fig. 13b. We observed about 36% reduction in carrier mobility to $0.2 \text{ cm}^2/\text{Vs}$ at the end of 120 days with a degradation rate of $26.90(\pm 2.48) \times 10^{-4} \text{ cm}^2/\text{Vs-day}$. However, the observed degradation rate significantly reduced from 120 days to 240 days. Such device degradation could be due to the continuous exposure of different gaseous molecules in ambient conditions and the oxidation of metal contacts.

Device Flexibility Test The flexibility of devices is a crucial requirement for many wearable applications [45]. The PET substrate-based OFETs are mechanically flexible. The device characteristics of the encapsulated OFETs fabricated on $10 \mu\text{m}$ PET substrates have been measured under tensile and compressive bending conditions in ambient conditions. The respective transfer characteristics of devices are shown in Fig. 14a and 14b. The variation of device mobility with different bending radius is presented in Fig. 14c. The device field-effect mobility is the same up to 4 mm bending condition. However, the devices work until the bending radius of 2 mm at the cost of about 60% reduction in carrier mobility. The device's performance during bending is degraded due to the formation of defect states or cracks generated on bending conditions [46].

Effect of Temperature on Device Performances The OFETs have been developed for sensing temperature. To check the temperature dependency, we have taken transfer characteristics at various temperatures from $20 \text{ }^\circ\text{C}$ to $50 \text{ }^\circ\text{C}$ with an interval of $5 \text{ }^\circ\text{C}$. The corresponding transfer curves for glass and PET substrate-based devices have been shown in Fig. 15a and b, respectively. The I_{DS} increases linearly with temperature. Such variation of device current for maximum V_{GS} and V_{DS} (for glass $V_{\text{GS}} = -1.0 \text{ V}$ and $V_{\text{DS}} = -1.0 \text{ V}$ and PET substrate $V_{\text{GS}} = -1.5 \text{ V}$ and $V_{\text{DS}} = -1.5$) with temperature is shown in Fig. 15c and 15d. The measured temperature range covers the human body temperature. Therefore, the OFET-based temperature sensors can be used for monitoring body temperature. The thermal sensitivity of the

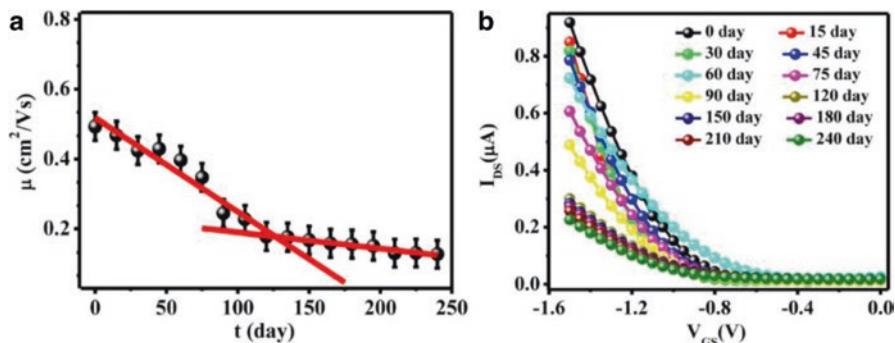


Fig. 13 presents the time-dependent (a) mobility and (b) transfer characteristics variation in days. (Reprinted from [19] © 2019 American Chemical Society)

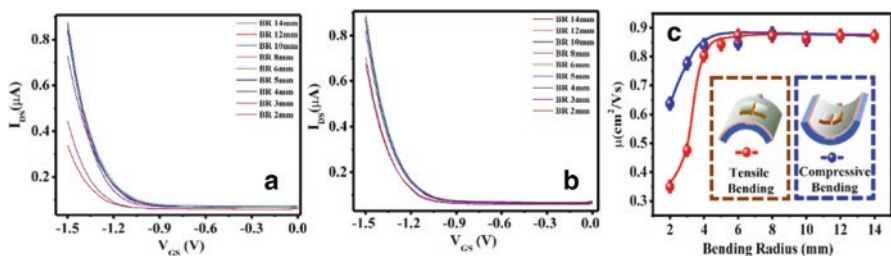


Fig. 14 shows transfer characteristics of the device (a) under tensile bending condition and (b) under compressive bending condition. (c) depicts the variation of device mobility during tensile as well as compressive bending conditions. (Reprinted from [19] © 2019 American Chemical Society)

sensors calculated from the slope of Fig. 15c and 15d for glass and PET substrates-based device is $36.8 (\pm 2.9) \text{ nA}/^\circ\text{C}$ and $30.6 (\pm 1.1) \text{ nA}/^\circ\text{C}$, respectively, within the temperature range of 20°C to 50°C .

We have measured the temperature-dependent device current responses for both sets of devices fabricated on glass and PET substrates. Figure 16a showed a typical response at different temperatures at a constant bias of $V_{DS} = -1.5 \text{ V}$ and $V_{GS} = -1.5 \text{ V}$ for glass substrates. Similar responses for the devices fabricated on PET substrates-based device with $V_{DS} = -1.2 \text{ V}$ and $V_{GS} = -1.2 \text{ V}$ are shown in Fig. 16c. To confirm the sensitivity of the thermal sensor around body temperature ($\sim 37^\circ\text{C}$), we have measured the responses at a temperature range covering body temperature. The typical responses are shown in Fig. 16b and 16d for glass and PET substrate-based devices, respectively. These results confirm the suitability of the OFETs as temperature sensors for wearable healthcare applications.

We have encapsulated the devices with a thick Polydimethylsiloxane (PDMS) film to prevent degradation in ambient conditions. The extra PDMS layer introduces heat loss while measuring temperature using this sensor. We have measured the

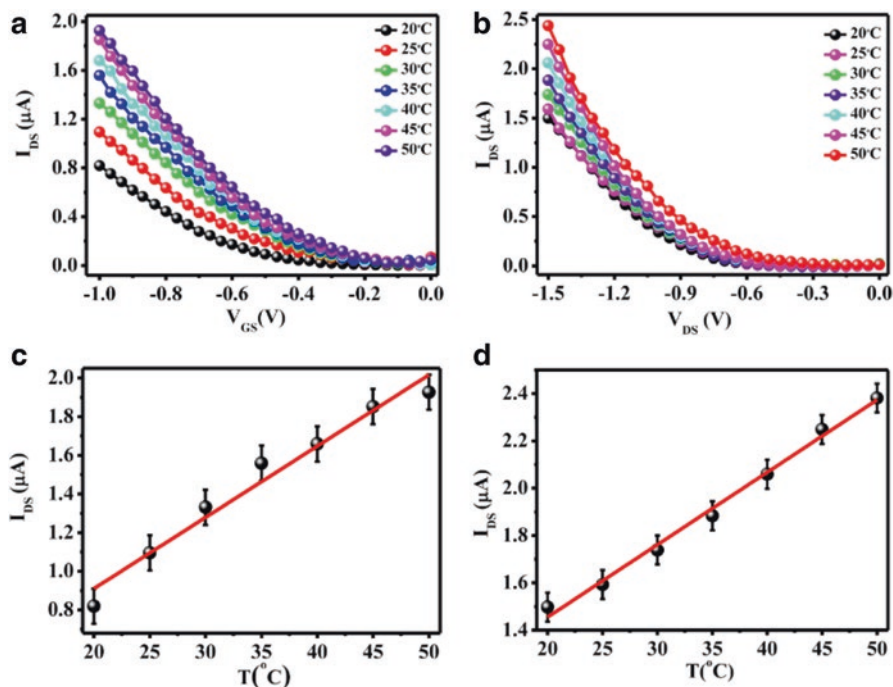


Fig. 15 Temperature-dependent transfer characteristics (a) for glass substrate working within 1.0 V and (b) for plastic substrate working within 1.5 V. The extracted device current from transfer characteristics as a function of temperature for (c) glass substrate at $V_{DS} = -1.0$ V and $V_{GS} = -1.0$ V and (d) plastic substrate at $V_{DS} = -1.5$ V and $V_{GS} = -1.5$ V over a range from 20 $^{\circ}\text{C}$ to 50 $^{\circ}\text{C}$

temperature response from the back and front sides of 100 μm PET substrate-based OFETs. Figure 17a and 17b shows the typical temperature responses taken from the devices for touching it on the PDMS layer and the PET substrate, respectively. The temperature response seems to be the same from both backsides of PET substrates and the PDMS coated side. This effect is mainly due to the similar thermal conductivity of 0.15 W/mK of PDMS and PET materials [47, 48]. So, the heat loss for both the materials would be similar, as observed in this case. The corresponding response and recovery process of such 70 repeated cycles are shown in Fig. 17b. The inset of the figure shows one individual response. The optical image of that device is shown in Fig. 17c, during the performance of the above measurements. Figure 17d presents the array of flexible OFET suitable for measuring special temperature variation in wearable applications.

The response time and recovery time are essential parameters in this OFET-based temperature sensors. We used the sensor to monitor the temperature difference of inhaling and exhaling air during breathing to measure response and recovery time. The temperature of the inhaled air is mainly room temperature (26.5 $^{\circ}\text{C}$). However, the exhaled air is primarily due to CO_2 coming out of the body. We have observed an almost 2 $^{\circ}\text{C}$ temperature difference between inhaled and exhaled air.

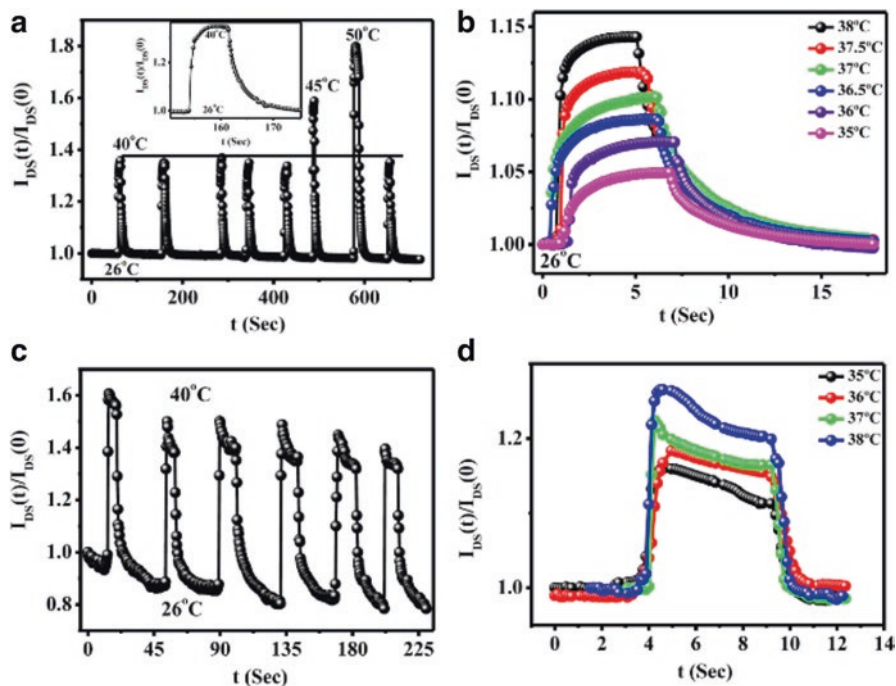


Fig. 16 The variation of device current with time measured during the change in temperature from (a) 26 °C to 40 °C, 45 °C, and 50 °C where Inset shows individual temperature response from 26 °C to 40 °C and (b) 26 °C to 35 °C, 36 °C, 36.5 °C, 37 °C, 37.5 °C, and 38 °C for glass substrate at constant $V_{DS} = -1.5$ V and $V_{GS} = -1.5$ V. Device current response for the temperature change from (c) 26 °C to 45 °C (d) 26 °C to 35 °C, 36 °C, 37 °C, and 38 °C for PET substrate-based device at constant $V_{DS} = -1.2$ V and $V_{GS} = -1.2$ V

We have measured the response of the devices from the speedy breathing exercises, as shown in Fig. 18a. One such individual temperature response profile is shown in Fig. 18b. The measured response time and recovery time from this device are about 24 ms and 51 ms, respectively.

To demonstrate the functionality of the temperature sensors for continuous monitoring of the body temperature, we have measured the variation of body temperature of mice during mild anesthesia. The body temperature of mice also was continuously monitored by this sensor under a mild dose of anesthesia. It is well known that mammals' body temperature falls by a few degrees when anesthesia is given. We mounted the sensor on the cleaned chest of mice. Two mild doses of anesthesia were given within a short time duration. We observed how the mice recover the body temperature with time. The corresponding variation of body temperature of the mice is shown in Fig. 18c. We have observed that the mice's body temperature decreased by 3–4 °C due to the anesthesia dose. The recovery process also has been monitored continuously, as shown in Fig. 18c. It has been found that the sensor can measure ultralow temperature variation of the mice while recovering

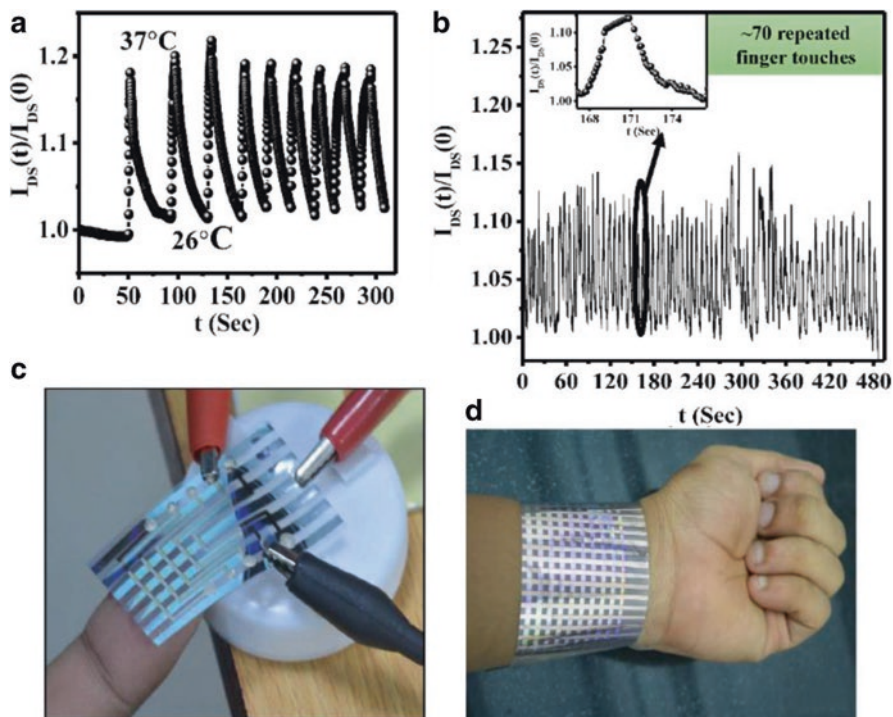


Fig. 17 Body temperature response from the encapsulating device upon touching the sensor from (a) front (PDMS) and (b) back (PET) side. One such cycle is shown in the inset Figure (b). (c) presents the optical image of the device during the measurement time. (d) shows the image of a flexible OFET-based array. (Reprinted from [19] © 2019 American Chemical Society)

from anesthesia. The sensor's precession was calculated from the linear part of A and B regions, as marked in the inset of Fig. 18c. The measured precession in temperature for this temperature sensor is 4.3 mK. The typical optical image of the temperature sensor mounted on the mice's chest during the experiment is shown in Fig. 18d.

7 Conclusions

This article discussed the synthesis of temperature-sensitive h-BTNCs sols using a low-cost solution process and has been used it for the fabrication of OFET-based flexible temperature sensors. We have covered from material characterization to fabrication of OFET through the various steps of optimizations of device parameters. The devices were found to be highly sensitive temperature sensors with 24 ms response time and 4.3 mK precession. Besides, the devices' power consumption is very low ($\sim 1 \mu\text{W}$), working at 1.5 V operating voltage. We have demonstrated the

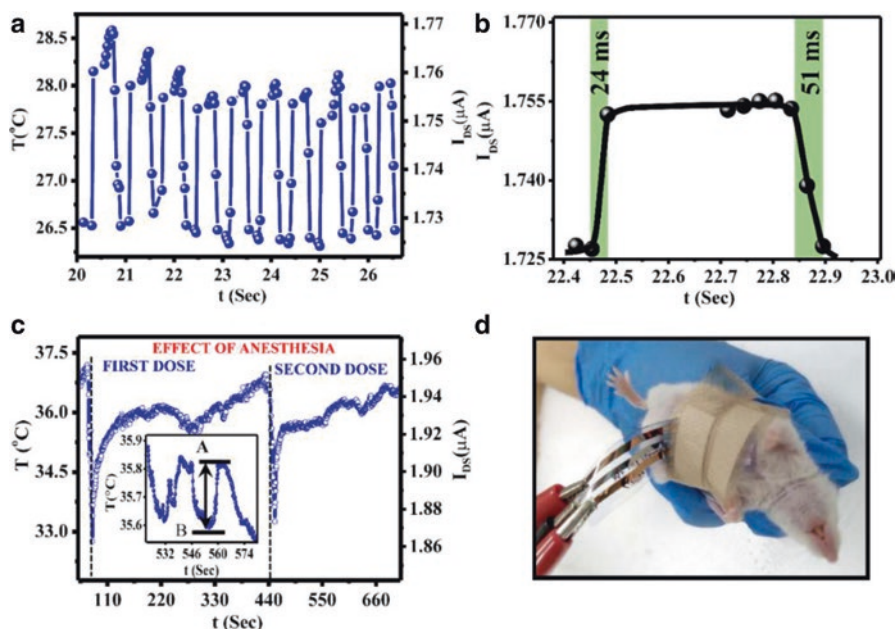


Fig. 18 (a) depicts fast breathing response measurements of the temperature sensor biased at V_{GS} and V_{DS} of -1.20 V. (b) shows one individual fast temperature response was taken from Figure (a). (c) presents body temperature variation of mice during anesthesia. The magnified view of the temperature variation taken in a different scan with higher time resolution shown in the inset of Figure (c). (d) illustrates a typical picture of a temperature sensor mounted in the mice during the experiment. (Reprinted from [19] © 2019 American Chemical Society)

use of the sensors for measuring body temperature. The flexibility of the device has been tested over 100 bending cycles with the smallest bending radius of 4 mm within which device property remains unchanged. We have also demonstrated that devices can monitor human beings' respiratory rate and can be suitable for detecting diseases like sleep apnea, asthma, and COPD.

Acknowledgments This work has been partially supported by various funding agencies of Government of India with sanction no: (MeitY) 5(1)/2017-NANO, (DST) DST/NM/NNetRA/2018(G) – IIT-KGP.

References

1. B.K.C. Kjellander, W.T.T. Smaal, K. Myny, J. Genoe, W. Dehaene, P. Heremans, G.H. Gelinck, Optimized circuit design for flexible 8-bit RFID transponders with active layer of ink-jet printed small molecule semiconductors. *Org. Electron.* **14**, 768–774 (2013)
2. V. Subramanian, P.C. Chang, J.B. Lee, S.E. Molesa, S.K. Volkman, Printed organic transistors for ultra-low-cost RFID applications. *IEEE Trans. Adv. Packag.* **28**, 742–747 (2005)

3. S.J. Kim, J.S. Lee, Flexible organic transistor memory devices. *Nano Lett.* **10**, 2884–2890 (2010)
4. S. Lee, H. Seong, S.G. Im, H. Moon, S. Yoo, Organic flash memory on various flexible substrates for foldable and disposable electronics. *Nat. Commun.* **8**, 725 (2017)
5. T. Sekitani, T. Yokota, U. Zschieschang, H. Klauk, S. Bauer, K. Takeuchi, M. Takamiya, T. Sakurai, T. Someya, Organic nonvolatile memory transistors for flexible sensor arrays. *Science* **326**, 1516–1519 (2009)
6. H. Fukagawa, T. Sasaki, T. Tsuzuki, Y. Nakajima, T. Takei, G. Motomura, M. Hasegawa, K. Morii, T. Shimizu, Long-lived flexible displays employing efficient and stable inverted organic light-emitting diodes. *Adv. Mater.* **30**, 1706768 (2018)
7. C.D. Sheraw, L. Zhou, J.R. Huang, D.J. Gundlach, T.N. Jackson, M.G. Kane, I.G. Hill, M.S. Hammond, J. Campi, B.K. Greening, J. Francl, J. West, Organic thin-film transistor-driven polymer-dispersed liquid crystal displays on flexible polymeric substrates. *Appl. Phys. Lett.* **80**, 1088–1090 (2002)
8. J. Smith, R. Hamilton, M. Heeney, D.M. de Leeuw, E. Cantatore, J.E. Anthony, I. McCulloch, D.D.C. Bradley, T.D. Anthopoulos, High-performance organic integrated circuits based on solution processable polymer-small molecule blends. *Appl. Phys. Lett.* **93**, 253301 (2008)
9. B. Crone, A. Dodabalapur, Y.Y. Lin, R.W. Filas, Z. Bao, A. LaDuca, R. Sarpeshkar, H.E. Katz, W. Li, Large-scale complementary integrated circuits based on organic transistors. *Nature* **403**, 521–523 (2000)
10. Y. Takeda, Y. Yoshimura, Y. Kobayashi, D. Kumaki, K. Fukuda, S. Tokito, Integrated circuits using fully solution-processed organic TFT devices with printed silver electrodes. *Org. Electron.* **14**, 3362–3370 (2013)
11. A. Chortos, J. Liu, Z.A. Bao, Pursuing prosthetic electronic skin. *Nat. Mater.* **15**, 937–950 (2016)
12. X.D. Wang, L. Dong, H.L. Zhang, R.M. Yu, C.F. Pan, Z.L. Wang, Recent progress in electronic skin. *Adv. Sci.* **2**, 1500169 (2015)
13. C. Xie, F. Yan, Flexible photodetectors based on novel functional materials. *Small* **13**, 1701822 (2017)
14. X.D. Liu, Y.W. Lin, Y.J. Liao, J.Z. Wu, Y.H. Zheng, Recent advances in organic near-infrared photodiodes. *J. Mater. Chem. C* **6**, 3499–3513 (2018)
15. S. Khan, S. Ali, A. Bermak, Recent developments in printing flexible and wearable sensing electronics for healthcare applications. *Sensors (Basel)* **19**, 1230 (2019)
16. G. Nan, Q. Shi, Z. Shuai, Z. Li, Influences of molecular packing on the charge mobility of organic semiconductors: From quantum charge transfer rate theory beyond the first-order perturbation. *Phys. Chem. Chem. Phys.* **13**, 9736–9746 (2011)
17. H. Zhang, X. Guo, J. Hui, S. Hu, W. Xu, D. Zhu, Interface engineering of semiconductor/dielectric heterojunctions toward functional organic thin-film transistors. *Nano Lett.* **11**, 4939–4946 (2011)
18. J. Liu, H.T. Zhang, H.L. Dong, L.Q. Meng, L.F. Jiang, L. Jiang, Y. Wang, J.S. Yu, Y.M. Sun, W.P. Hu, A.J. Heeger, High mobility emissive organic semiconductor. *Nat. Commun.* **6**, 10032 (2015)
19. S. Mandal, M. Banerjee, S. Roy, A. Mandal, A. Ghosh, B. Satpati, D.K. Goswami, Organic field-effect transistor-based ultrafast, flexible, physiological-temperature sensors with hexagonal barium titanate nanocrystals in amorphous matrix as sensing material. *ACS Appl. Mater. Interfaces* **11**, 4193–4202 (2019)
20. T.Q. Trung, N.E. Lee, Flexible and stretchable physical sensor integrated platforms for wearable human-activity monitoring and personal healthcare. *Adv. Mater.* **28**, 4338–4372 (2016)
21. X. Wu, Y. Ma, G. Zhang, Y. Chu, J. Du, Y. Zhang, Z. Li, Y. Duan, Z. Fan, J. Huang, Thermally stable, biocompatible, and flexible organic field-effect transistors and their application in temperature sensing arrays for artificial skin. *Adv. Funct. Mater.* **25**, 2138–2146 (2015)
22. H. Li, W. Shi, J. Song, H.J. Jang, J. Dailey, J.S. Yu, H.E. Katz, Chemical and biomolecule sensing with organic field-effect transistors. *Chem. Rev.* **119**, 3–35 (2019)
23. J.N. Curti, K.L. Adriance, E.C. Land, in *Adaptive Temperature Sensor for Breath Monitoring Device*. US 8740808 (2017)

24. A.L. Dunlop, R. Schultz, E. Frank, Interpretation of the BBT chart: Using the “Gap” technique compared to the coverline technique. *Contraception* **71**, 188–192 (2005)
25. H.W. Su, Y.C. Yi, T.Y. Wei, T.C. Chang, C.M. Cheng, Detection of ovulation, a review of currently available methods. *Bioeng. Transl. Med.* **2**, 238–246 (2017)
26. B. Kudlak, N. Jatkowska, P. Kubica, G. Yotova, S. Tsakovski, Influence of storage time and temperature on the toxicity, endocrine potential, and migration of epoxy resin precursors in extracts of food packaging materials. *Molecules* **24**, 4396 (2019)
27. A.M. Karow, W.B. Gilbert, J.B. Black, Effects of temperature, potassium concentration, and sugar on human spermatozoa motility: a cell preservation model from reproductive medicine. *Cryobiology* **29**, 250 (1992)
28. S.M. Abdullah, Z. Ahmad, K. Sulaiman, A solution-based temperature sensor using the organic compound CuTsPc. *Sensors* **14**, 9878–9888 (2014)
29. F.T. Silva, B. Sorli, V. Calado, C. Guillaume, N. Gontard, Feasibility of a gelatin temperature sensor based on electrical capacitance. *Sensors* **16**, 2197 (2016)
30. H.Y. Ma, Q.A. Huang, M. Qin, T. Lu, A micromachined silicon capacitive temperature sensor for wide temperature range applications. *J. Micromech. Microeng.* **20**, 055036 (2010)
31. J. Jeon, H.B.R. Lee, Z. Bao, Flexible wireless temperature sensors based on Ni microparticle-filled binary polymer composites. *Adv. Mater.* **25**, 850–855 (2013)
32. S. Harada, K. Kanao, Y. Yamamoto, T. Arie, S. Akita, K. Takei, Fully printed flexible fingerprint-like three-axis tactile and slip force and temperature sensors for artificial skin. *ACS Nano* **8**, 12851–12857 (2014)
33. W. Honda, S. Harada, S. Ishida, T. Arie, S. Akita, K. Takei, High-performance, mechanically flexible, and vertically integrated 3D carbon nanotube and InGaZnO complementary circuits with a temperature sensor. *Adv. Mater.* **27**, 4674–4680 (2015)
34. T. Yokota, Y. Inoue, Y. Terakawa, J. Reeder, M. Kaltenbrunner, T. Ware, K.J. Yang, K. Mabuchi, T. Murakawa, M. Sekino, W. Voit, T. Sekitani, T. Someya, Ultraflexible, large-area, physiological temperature sensors for multipoint measurements. *Proc. Natl. Acad. Sci. U. S. A.* **112**, 14533–14538 (2015)
35. S.Y. Hong, Y.H. Lee, H. Park, S.W. Jin, Y.R. Jeong, J. Yun, I. You, G. Zi, J.S. Ha, Stretchable active matrix temperature sensor array of polyaniline nanofibers for electronic skin. *Adv. Mater.* **28**, 930–935 (2016)
36. X. Ren, K. Pei, B. Peng, Z. Zhang, Z. Wang, X. Wang, P.K.L. Chan, A low-operating-power and flexible active-matrix organic-transistor temperature-sensor array. *Adv. Mater.* **28**, 4832–4838 (2016)
37. T.Q. Trung, S. Ramasundaram, S.W. Hong, N.E. Lee, Flexible and transparent nanocomposite of reduced graphene oxide and P(VDF-TrFE) copolymer for high thermal responsivity in a field-effect transistor. *Adv. Funct. Mater.* **24**, 3438–3445 (2014)
38. T.Q. Trung, N.T. Tien, D. Kim, J.H. Jung, O.J. Yoon, N.E. Lee, High thermal responsiveness of a reduced graphene oxide field-effect transistor. *Adv. Mater.* **24**, 5254–5260 (2012)
39. C. Miot, E. Husson, C. Proust, R. Erre, J.P. Coutures, Residual carbon evolution in BaTiO₃ ceramics studied by XPS after ion etching. *J. Eur. Ceram. Soc.* **18**, 339–343 (1998)
40. S. Steudel, D.S. Vussera, D.S. Jonge, D. Janssen, S. Verlaak, J. Genoe, P. Heremans, Influence of the dielectric roughness on the performance of pentacene transistors. *Appl. Phys. Lett.* **85**, 4400 (2004)
41. S.E. Fritz, T.W. Kelley, C.D. Frisbie, Effect of dielectric roughness on performance of pentacene TFTs and restoration of performance with a polymeric smoothing layer. *J. Phys. Chem. B* **109**, 10574–10577 (2005)
42. M. Girtan, S. Dabos-Seignon, A.L. Stanculescu, On morphological, structural and electrical properties of vacuum deposited pentacene thin films. *Vacuum* **83**, 1159–1163 (2009)
43. Y. Jung, R.J. Kline, D.A. Fischer, E.K. Lin, M. Heeney, I. McCulloch, D.M. DeLongchamp, The effect of interfacial roughness on the thin film morphology and charge transport of high-performance polythiophenes. *Adv. Funct. Mater.* **18**, 742–750 (2008)

44. X.N. Sun, C.A. Di, Y.Q. Liu, Engineering of the dielectric-semiconductor interface in organic field-effect transistors. *J. Mater. Chem.* **20**, 2599–2611 (2010)
45. S. Patel, H. Park, P. Bonato, L. Chan, M. Rodgers, A review of wearable sensors and systems with application in rehabilitation. *J. Neuroeng. Rehabil.* **9**, 21 (2012)
46. V. Raghuvanshi, D. Bharti, S.P. Tiwari, Flexible organic field-effect transistors with TIPS-pentacene crystals exhibiting high electrical stability upon bending. *Org. Electron.* **31**, 177–182 (2016)
47. K. Uetani, T. Okada, H.T. Oyama, Crystallite size effect on thermal conductive properties of nonwoven nanocellulose sheets. *Biomacromolecules* **16**, 2220–2227 (2015)
48. P. Yi, R.A. Awang, W.S.T. Rowe, K. Kalantar-zadeh, K. Khoshmanesh, PDMS nanocomposites for heat transfer enhancement in microfluidic platforms. *Lab Chip* **14**, 3419–3426 (2014)